Solar Energy Materials and Solar Cells 174 (2018) 240–247

Contents lists available at ScienceDirect

Solar Energy Materials and Solar Cells

journal homepage: www.elsevier.com/locate/solmat

Surface fluorination of α-Fe_2O_3 using selectfluor for enhancement in photoelectrochemical properties

Vikash C. Janu[a,b], Gaurav Bahuguna[a], Devika Laishram[a], Kiran P. Shejale[a], N. Kumar[b], Rakesh K. Sharma[a,*], Ritu Gupta[a,*]

[a] Department of Chemistry, Indian Institute of Technology Jodhpur, Jodhpur, Rajasthan , 342037 India
[b] Defence Laboratory (DRDO), Jodhpur, Rajasthan 342011, India

ARTICLE INFO

Keywords:
Fluorination
Hematite
Bandgap
Photoelectrochemical cell
Dendritic
DSSC

ABSTRACT

Fluorinated α-Fe_2O_3 nanostructures are synthesized via a facile hydrothermal route using Selectfluor™ (F-TEDA) as a fluorinating as well as growth directing agent. The addition of incrementally increasing amount of F-TEDA to Fe precursor under hydrothermal conditions resulted in preferential growth of α-Fe_2O_3 along (110) orientation with respect to (104) direction by ~ 35%, the former being important for enhanced charge transport. On increasing fluorination, the heirarchical dendritic-type α-Fe_2O_3 changes to a snow-flake type structure (F-TEDA-20%) anisotropically growing along the six directions however, at higher F-TEDA concentrations ($\geq$ 30%), loosely held particulate aggregates are seen to be formed. The X-Ray Photoelectron Spectroscopy (XPS) suggest the maximum fluorinarion of α-Fe_2O_3 at 1.21 at% in 30% F-TEDA. Further, optical absorption studies reveal reduction in optical band gap from 2.10 eV in case of pristine to 1.95 eV for fluorinated α-Fe_2O_3. A photoanode made by taking 20% fluorinated α-Fe_2O_3 in a ratio of 10:90 with respect to TiO_2 (P-25) showed improved performance in dye sensitized solar cells with an increase in efficiency by ~16% in comparision to that of pristine Fe_2O_3 and TiO_2. Furthermore, anode consisting of thin films of fluorinated α-Fe_2O_3 on FTO also exhibit enhanced current density on illumination of ~100 W/m^2. The increase in photoelectrochemical activity seems to be due to the combination of two factors namely preferential growth of α-Fe_2O_3 along (110) direction resulting in an improved charge transfer efficiency and reduced recombination losses due to the presence of fluorine.

1. Introduction

Hematite or α-Fe_2O_3 is widely used in a variety of applications such as electrode in lithium batteries [1,2], production of magnetic materials [3], visible-light photocatalysis [4–6], water treatment [7], gas sensors [1,8], electromagnetic devices, paints and pigments [9]. High-quality hematite films are mainly fabricated by various techniques such as atmospheric pressure chemical vapor deposition (APCVD), atomic layer deposition, electron-beam, pulse laser deposition, reactive DC magnetron sputtering and metal organic decomposition for use in photoelectrochemical cells [10–13]. Being a highly abundant, low cost and non-toxic material with a low bandgap of 2.1–2.2 eV, α-Fe_2O_3 has attracted immense attention in the recent past. However, there are certain drawbacks that limits the use of α-Fe_2O_3 in solar application such as low mobility of carriers ($< 0.1\ cm^2V^{-1}s^{-1}$) [14] high recombination rates, short diffusion length (2–4 nm) [15], short excited state lifetime (< 10 ps) [16], poor light absorption [17], and improper band position [18] for unassisted water splitting that limit its application in solar applications. There is lot of impetus in improving its properties by structural modification, variation in morphology and by doping [19,20].

Recently, extrinsic fluorine anion doping of semiconducting metal oxides such as SnO_2, TiO_2, Co_3O_4 and Fe_2O_3 have turned out as an important route for surface passivation of metal oxides that inhibits e^-/h^+ recombination and improves charge carriers mobility. Additionally, fluorine doping is expected to achieve tunable optical absorption and modified band position for enhancement in photoelectrochemical activity. Theoretical studies also suggest that the partial replacement of O^{2-} by aliovalent anion such as F^- can effectively reduce the electrical resistivity of Fe_2O_3 [21]. For example, Tondello et al. synthesized F-doped Co_3O_4 by plasma enhanced chemical vapor deposition method using fluorinated β-diketonatecobalt derivative as a single fluorine and cobalt precursor and observed a significant improvement in hydrogen production. Similarly, Choi et al. carried out fluorination of TiO_2 using

---

* Corresponding authors.
E-mail addresses: rks@iitj.ac.in (R.K. Sharma), ritu@iitj.ac.in (R. Gupta).

http://dx.doi.org/10.1016/j.solmat.2017.09.006
Received 28 June 2017; Received in revised form 2 August 2017; Accepted 6 September 2017

sodium fluoride for enhanced photo catalytic action [22,23]. The enhancement in catalytic activity is understandable due to increase in Lewis acidity of Fe-centers by substitution of surface oxygen atoms with fluorine. For example, Zhu *et al.* observed rapid photo catalytic degradation of Rhodamine dye using fluorinated SnO_2 [24,25]. Several fluorine-doped metal oxides have been synthesized in order to enhance the electrochemical performance of energy storage devices. Lee et al. synthesized F, N-doped Fe_2O_3 using ammonium fluoride and urea and used it for supercapacitor application [26].

Among solution-based fluorinating agents, HF and NH_4F are generally used, however, these act preferentially as growth directing agents with no evidence for fluorination in the growth of metal oxides [27]. Herein, we for the first time, utilized F-TEDA as a fluorinating agent that provides electrophilic fluorine in solution as the reactive species. In this work, we developed a facile yet effective hydrothermal strategy for the in-situ preparation of F-Fe_2O_3 by modifying the known method for dendritic growth of α-Fe_2O_3 [28]. In order to understand the interaction of fluorine with α-Fe_2O_3, we focussed on the interplay between the fluorine content (varying F-TEDA concentration 0–40%) and resulting structural, optical and photoelectrochemical properties together with study on its application in visible light photo-electrochemical and dye sensitized solar cells.

2. Experimental section

2.1. Synthesis of pristine and F-Fe_2O_3

Aqueous solution of (15 mM) of $K_3[Fe(CN)_6]$ was heated in Teflon hydrothermal vessel (200 mL) at 140 °C for 48 h following the literature method [28]. The precipitate was obtained and washed with de-ionized (DI) water followed by ethanol wash to get rid of the by-products. It was further centrifuged and dried in hot air oven at 70 °C for 4h. *In-situ* fluorination was carried out using Selectfluor™ (N-Chloromethyl-N′-fluorotriethylenediammoniumbis(tetrafluoroborate), F-TEDA, Sigma Aldrich) as the fluorinating agent. F-TEDA was mixed in different weight percent with respect to the principal reactant before the start of reaction.

2.2. Characterization

Bruker D8 Advance diffractometer equipped with Cu-Kα radiation having 1.54 Å wavelength was used for X-ray diffraction (XRD) analysis. ^{19}F NMR spectra were collected from the reaction mixture before and after reaction (supernatant) in D_2O using Bruker 500 spectrometer operating at 500 MHz. TEM imaging was performed by transmission electron microscope (FEI Technai G2 T20 ST) equipped with energy-dispersive X-ray spectroscopy (Burker X-100). For imaging, ~10 mg of sample was dispersed in ethanol and drop casted on a copper grid and allowed to dry before imaging. HRTEM images were analyzed using Image J and Gatan digital micrograph software. Field Emission Scanning Electron Microscope (FESEM) imaging was performed using Nova NanoSEM 600 instrument (FEI Co., The Netherlands). Diffuse reflectance spectra were recorded in solid state using UV–vis spectrophotometer (Varian Cary 4000) with polytetrafluoroethylene (PTFE) as the reference material. Surface composition and chemical states were measured with an Omicron nanotechnology (Oxford instruments) X-ray photoelectron spectroscopy (XPS) instrument equipped with monochromatic Al Kα radiation. Specific surface area was analyzed by N_2 adsorption–desorption isotherms (Quntachrome autosorb iQ3). Solar Simulator (model number SS50AA, Photoemission Tech) was used to illuminate the devices.

2.3. DSSC fabrication

All solar cells were prepared according to the typical procedure as mentioned in our previous study [29]. Briefly, pristine and F-Fe_2O_3 (20%) were mixed with TiO_2 (P25) powders in 5:95, 10:90, 20:80 and 40:60 ratios in the form of a paste and uniformly grinded with ethyl cellulose in α-terpinol and ethanol (wt% ratio: 2.7:1:3.38). The paste was screen printed on the fluorine doped tin oxide (FTO) substrates and dried at 120 °C for 6 min and repeatedly printed 5 times to increase the layer thickness. The electrodes were sintered at 450 °C for 30 min in the air resulting in film of ~15 µm thickness with active area of 1 cm^2. The platinum sol was deposited onto the FTO counter electrode and then calcined at 450 °C for 30 min. The photoanodes were soaked in 0.5 mM N719 dye solution for 18 h. Finally, these were assembled along with Pt counter electrode using a Surlyn spacer (thickness of 25 µm) and Iodolyte Z 50 (Solaronix) as the electrolyte resulting in a sandwich structure as shown in supporting information, Fig. S2a. The fabricated DSSC device was then illuminated under solar simulator 1000 W/m^2 (1 Sun) for J-V and EIS measurements. All the fabricated DSSCs were averaged over three cells.

2.4. Photoelectrochemical measurements

The films of α-Fe_2O_3 and F-Fe_2O_3 were prepared by three layer screen printing on FTO glass for photoelectrochemical measurements. The paste of appropriate viscosity was prepared by mixing 0.05 g of ethyl cellulose, 0.3 mL of α-terpinol and 0.02 mL glacial acetic acid in a mortar and pestle for 30 min. Upon complete dissolution of ethyl cellulose, 0.1 g of hematite was added and mixed for 10 min. Further, appropriate amount of ethanol was added for viscosity adjustment. The prepared paste was layer by layer coated on FTO glass using 100 mesh screen and squeegee. Every layer was dried before coating successive layer. The prepared films were further annealed at 500 °C for 5 h before using for electrochemical measurements. Electrochemical workstation (CHI6600) was used for I-V measurements and impedance spectroscopy (EIS) analysis in a three-electrode set up using Pt mesh as counter electrode and Ag/AgCl (3 M KCl) as reference electrode. The potential were converted to the reversible hydrogen electrode (RHE) scale using the standard Nernst equation. The graphs were plotted from a frequency range of 1–10^5 Hz. Chronoamperometry experiments were performed at 0.6 V versus Ag/AgCl (1.6 V versus RHE). The measurements were performed under illumination of 100 W/m^2 (one-tenth of 1 Sun) while the light source was switched on and off after every 5 s. The photocurrent value at the end of the chronoamperometry measurement was taken as the steady-state photocurrent and was used to compare different samples.

3. Results and discussion

F-TEDA is a well-known, commercially available, stable fluorinating reagent that acts as a source of *electrophilic fluorine* in organic synthesis [30–32]. In this study, we have employed it for fluorination of an inorganic material, α-Fe_2O_3 not only due to its high reactivity but also for its ease of handling as compared to the other sources of fluorine such as HF, XeF_2 and F_2 [33,34]. Synthesis is scaled up in different-sized Teflon vessels of 100, 200 and 800 mL capacity as shown in Fig. 1a. The hydrothermal reaction for $K_3[Fe(CN)_6]$ was carried out with and without F-TEDA at an optimized reaction condition of ~140 °C for 48 h as detailed in experimental methods. The pH changes in the reaction medium were monitored before and after reaction completion to gain better insight in the process of fluorination (Fig. 1c). The pH of the reaction mixture containing Fe precursor and F-TEDA (10 wt% − 40 wt %) is comparatively lower (pH = 3.4 − 4.0) than Fe precursor in water (pH = 6.2) as the F-TEDA is a salt of strong acid and weak base. However, after the hydrothermal reaction, pH of the supernatant becomes higher due to CN^- assisted dissociation of water that result in formation of OH^- ions [35]. For higher concentrations of F-TEDA, the pH of supernatant after the reaction decreases gradually. As seen from Fig. 1c (bottom curve), the overall pH change for the reaction is higher in presence of fluorinating agent (10, 20 and 30 wt% of F-TEDA) as

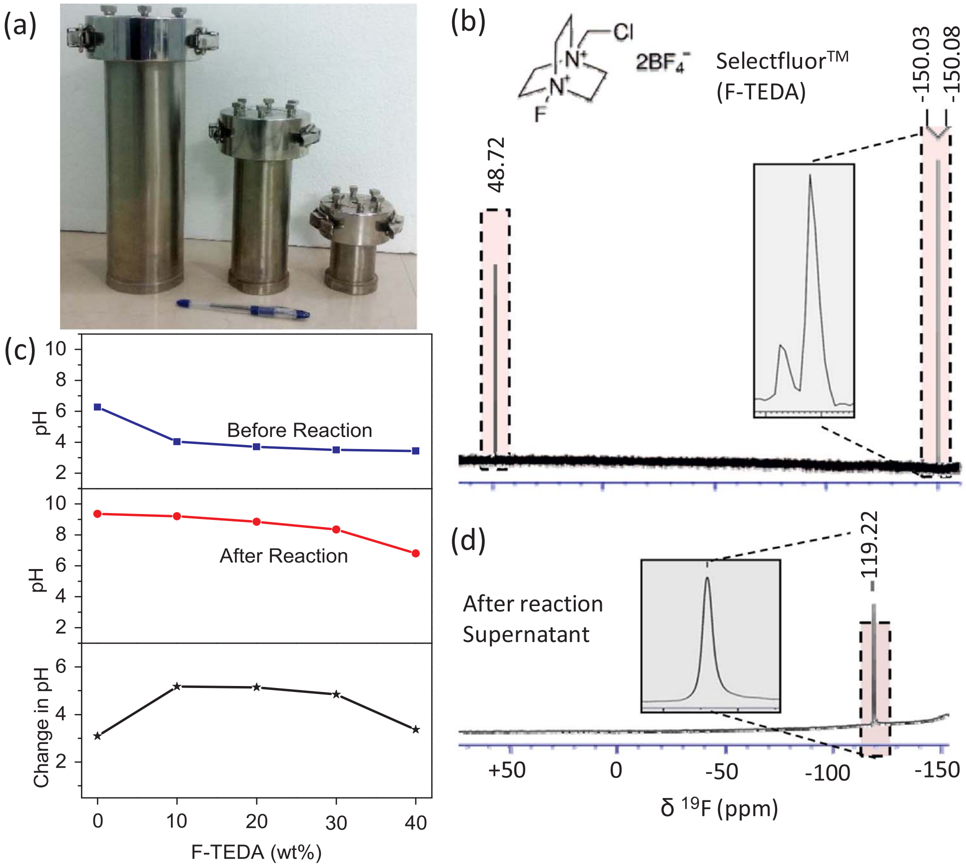

Fig. 1. (a) Digital photograph of the hydrothermal vessels of 800 mL, 200 mL and 100 mL capacity used for scale-up synthesis of pristine and F-Fe_2O_3. (b) pH changes before and after reaction for increasing concentration of F-TEDA.F-19 NMR spectra of the reaction medium, (c) before and (d) after reaction (from supernatant).

compared to pristine. With higher F-TEDA (40 wt%), overall pH change after reaction is similar to pristine due to neutralization of hydroxide ions by excess of F-TEDA. Here, F-TEDA plays an important role in influencing the pH of the reaction medium and thus the growth of Fe based nanostructures. The complete mechanism of F-TEDA reaction with $K_3[Fe(CN)_6]$ under hydrothermal condition is difficult to elucidate. However, NMR studies were performed externally to verify the release of electrophilic F^+ in the reaction mixture. The NMR spectrum of F-TEDA shows a peak at +48.7 ppm corresponding to N–F bond (F^+ species) and doublet at −150.3 and −150.8 ppm (two BF_4 anion) as shown in Fig. 1b. After the reaction, the peak at +48.7 ppm corresponding to the F^+ species disappears while the doublet from BF_4 anion at ~150 ppm shifts to 119.2 ppm due to the change in environment of BF_4 anions after the liberation of F^+ from F-TEDA during the hydrothermal reaction (Fig. 1d).

The pristine and F-Fe_2O_3 synthesized under identical growth conditions are characterized by FESEM and TEM imaging (Fig. 2). The pristine α-Fe_2O_3 has a typical dendrite type structure (Figs. 2a and 2f) with the backbone oriented in [1$\bar{1}$00] direction. The surface and structure of α-Fe_2O_3 undergoes modification by systematic introduction of F-TEDA in the reaction mixture. At 10% F-TEDA, some of the dendrite structures start assembling along four directions (Figs. 2b and 2g). When 20% F-TEDA was added to the reaction mixture, α-Fe_2O_3 exhibited a clear change in shape from single dendrite to snow flake-type nanostructure with six-fold symmetry (Figs. 2c and 2h). At much higher F-TEDA concentration (30% or more), the growth rate is accelerated in all crystallographic directions resulting in loose aggregates of nanoparticles (Figs. 2d, 2e, 2i and 2j). The α-Fe_2O_3 synthesized with 20% of F-TEDA is further examined in detail. The electron diffraction pattern with zone axis [0001] shows the hexagonal reciprocal lattice of the corresponding snowflake-type structure. The inter-planar distance of 0.2528 nm corresponds to the {11$\bar{2}$0} family of planes growing in [1$\bar{1}$00] family direction (Fig. 2k and 2l). The EDS maps of Fe-Kα, O-Kα and F-Kα corresponding to the TEM images in Figs. 2m,n and o exhibit uniformly distributed signals indicating that fluorine is uniformly covering the surface of α-Fe_2O_3.

The phase, crystallinity and orientation of α-Fe_2O_3 before and after fluorination was examined by Powder X-ray diffraction (Fig. 3a). All the peaks in the XRD pattern for pristine as well as F-Fe_2O_3 (JCPDS 33–0664). This indicates that there is no change in the phase or composition and it is only surface fluorination. The intense and broad peaks are evident of nanocrystalline nature of α-Fe_2O_3. Neither new peaks nor any shift in position of peaks could be observed for F-Fe_2O_3 since F^- has a similar ionic radius (133 pm) with that of O^{-2} (140 pm) resulting in negligible lattice distortion [36]. The average crystallite size is ~35.6 nm, calculated from highest intense peak using Scherrer equation. The crystallite size of F-Fe_2O_3 is similar to average crystallite size of the pristine α-Fe_2O_3 (Table S1). It can be observed that with increase in F-TEDA concentration used for fluorination of α-Fe_2O_3, there is a linear increase in growth along [110] direction as seen by the increase in (110) diffraction peak with respect to (104) peak intensity (Fig. 3b). The (110) orientation of α-Fe_2O_3 is known to posses anisotropic conductivity much higher than (104) orientation due to closed-packing (inset, Fig. 3b) resulting in improved charge collection of photo-excited charge carrier [37–39]. Therefore, the F-Fe_2O_3 is expected to have better potential for water splitting.

In order to confirm the presence of fluorine, a detailed XPS analysis of pristine and F-Fe_2O_3 was performed (Fig. 4). The XPS full range survey scan show signals corresponding to Fe 2p and Fe 3s, O 1s and C 1s along with an additional low count signal for F 1s in F-Fe_2O_3 (Fig. S1). Upon fluorination, a downward shift in BE values is observed for Fe 2p and O 1s signals successively in all cases (Fig. 4a and b) due to changes in the chemical state upon fluorine binding [40]. Pristine α-Fe_2O_3 shows a doublet peak at ~723.1 eV and 709.6 eV that correspond to Fe $2p_{1/2}$ and Fe $2p_{3/2}$ respectively with an energy split of ~13.5 eV which is consistent with the reported value of Fe^{+3} in pristine α-Fe_2O_3

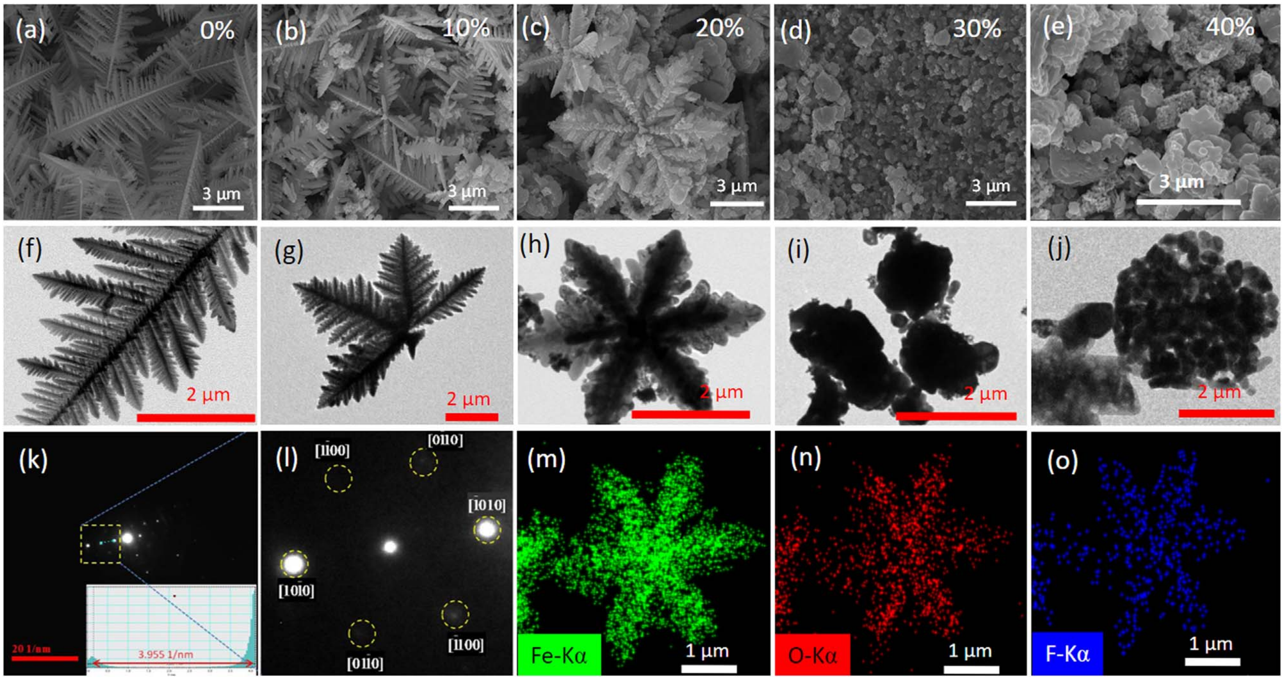

Fig. 2. (a-e) Field-Emission Scanning Electron Microscope images and corresponding (f-j) Transmission Electron Microscopy images of pristine and F-Fe_2O_3 with 10%, 20%, 30% and 40% of F-TEDA respectively. (k, l) Selected Area Electron Diffraction pattern at low and high magnification and (m-o) Energy Dispersive Spectroscopy (EDS) imaging of F-Fe_2O_3 with 20% F-TEDA.

[26]. Fe $2p_{1/2}$ and Fe $2p_{3/2}$ signals in F-Fe_2O_3 (F-TEDA of 10% − 40%) are slightly shifted with increasing fluorine content (Table 1). Pristine α-Fe_2O_3 upon de-convolution of O 1s shows two peaks at 529.6 eV and 532.1 eV corresponding to lattice oxide and surface hydroxide respectively (Fig. 4b) [41]. F-Fe_2O_3 (10–40%) exhibit prominent O 1s surface hydroxide signals that may be attributed to favorable formation of surface hydroxides due to fluorination. The core-level F 1s signal is weak and could not be noticed in 10 wt% F-TEDA however a broad and tiny peak appeared at ~ 683 eV for 20% and higher wt% of F-Fe_2O_3, thus confirming surface fluorination of Fe_2O_3 (Fig. 4c). The quantitative estimation of fluorine shows 0.41 at%, 1.21 at% and 1.13 at% of fluorine for Fe_2O_3 synthesized with 20%, 30% and 40% weight of F-TEDA respectively (Table 1). As seen in literature (see Table S2), the F 1s signal due to surface binding occurs at lower BE values (~683 eV) while doping of fluorine in solid solution results in BE shift at higher values (~688 eV) [42]. Interestingly, the peak at ~ 683 eV indicates the possibility of surface fluorination by fluoride formation and hydroxide ligand exchange at surface [23,26]. Since there is no F 1s signal at ~ 688 eV, the fluoride doping in solid solution is not accounted in this study.

In order to elucidate the effect of surface fluorination on optical properties of α-Fe_2O_3, the UV–vis diffuse reflectance spectra are recorded for pristine and F-Fe_2O_3 (Fig. 5a, inset). The band edge in Tauc plot is extrapolated to the *x*-axis for obtaining the band gap of pristine and F-Fe_2O_3 samples. The corresponding bandgaps were obtained from the modified Kubelka–Munk function, as shown in Fig. 5a. It can be seen that bandgap of F-Fe_2O_3 gradually decreases as compared to pristine α-Fe_2O_3 (Fig. 5b) which is in agreement with their lower reflectance in Fig. 5a (inset). This may be attributed to improved surface electrical conductivity of F-Fe_2O_3. The direct band gap derived for pristine α-Fe_2O_3 (2.09 eV) matches well with literature band gap values 2.0–2.2 eV. This optical absorption in the visible spectrum demonstrated that F-Fe_2O_3 has immense potential as photoanode material. Since, an ideal photoanode requires suitable band gap large enough ($>$ 1.6 eV) to split water and faster electron transport and small enough (2.2 eV) to absorb a wide range of the solar spectrum, F-Fe_2O_3 is tested for photo-electrochemical cells.

α-Fe_2O_3 has been used as photo-anode as well as counter-electrode in dye sensitized solar cells [43,44]. α-Fe_2O_3 as photoanode is not much exploited due to its poor charge carrier mobility (see literature reports in Table S3) [5]. However, fluorinated α-Fe_2O_3 enhances charge transfer efficiency due to preferential growth of α-Fe_2O_3 in 110 plane

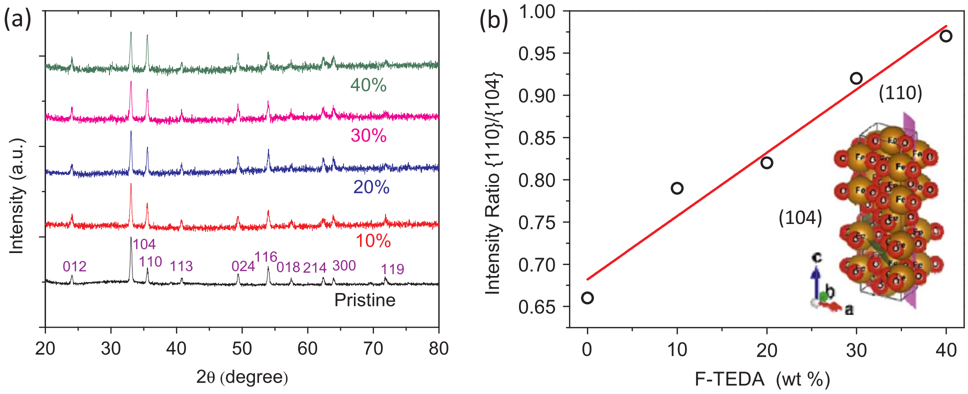

Fig. 3. (a) P-XRD patterns and corresponding (b) Variation in intensity of {110/104} peak ratio with respect to weight% of F-TEDA. Inset in b the packing of atoms in both (110) and (104) crystallographic planes.

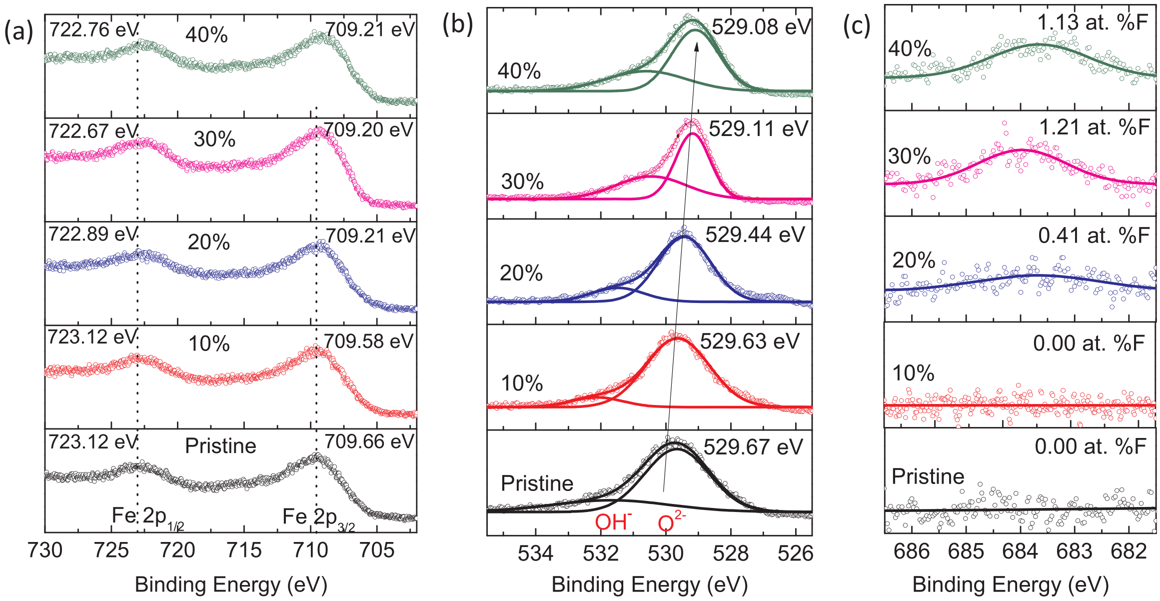

Fig. 4. X-ray photoelectron spectra (XPS) of (a) Fe 2p (b) O 1s and (c) F 1s of pristine α-Fe_2O_3 and F-Fe_2O_3. Note that the peak values are calibrated with reference to carbon at 284.8 eV.

Table 1
Elemental quantification of Fe, O and F in pristine and F-Fe_2O_3. Note that the peak values are calibrated with reference to adventitious carbon at 284.8 eV. ND refers to not defined indicating absence of peak.

F-TEDA (%)	Fe 2p		O 1s		F 1s	
	BE (eV)	at%	BE (eV)	at%	BE (eV)	at%
0	709.66	33.57	529.67	66.43	ND	0
10	709.58	33.57	529.63	66.43	ND	0
20	709.21	33.35	529.44	66.24	683.59	0.41
30	709.2	32.94	529.11	65.85	683.95	1.21
40	709.21	32.94	529.08	65.93	683.62	1.13

compared to pristine α-Fe_2O_3 (Fig. 3). To see the increase in charge transfer efficiency contribution of fluorine, fluorinated and pristine α-Fe_2O_3 is combined with TiO_2 photoanode for fabrication of DSSC devices (Fig. S2a). F-Fe_2O_3 with TiO_2 together can absorb in entire UV and visible spectrum and as a result provide more photoelectrons for improved light harvesting (Fig. S2b). The TiO_2 is mixed in different ratios to optimize the number of sites for dye adsorption as well as light harvesting for maximum photo-conversion efficiency. DSSCs were fabricated using different fractions of F-Fe_2O_3 (F-TEDA-20%) and pristine α-Fe_2O_3 with TiO_2 as photoanode material for optimized performance. Eight different sets of DSSCs were fabricated for different combinations of photoanode and their photovoltaic parameters are given in Table S4. The photocurrent density versus voltage (J-V) curves of the DSSCs fabricated with various proportions of pristine and F-Fe_2O_3 with TiO_2 (5:95, 10:90, 20:80 and 40:60) are shown in Figs. 6a and 6b. DSSCs fabricated from pristine and F-Fe_2O_3:TiO_2 of 10:90 ratio exhibit maximum power conversion efficiency, η of 3.41% and 2.75% beyond which it decreases probably due to higher reflectance from F-Fe_2O_3 (Fig. 6c). In comparison, DSSC was fabricated from TiO_2(P25) and reported 1.2% PCE (Fig. S3).

The power conversion efficiency η (%) in case of F-Fe_2O_3: TiO_2 (10:90) is higher than pristine Fe_2O_3 mixture by ~16% probably due to the higher dye intake in F-Fe_2O_3 due to modified surface properties despite of decrease in BET surface area of pristine α-Fe_2O_3 upon fluorination (41.2 m^2/g for pristine while 9.83 m^2/g for α-Fe_2O_3 with 20% F-TEDA concentration) as shown in Fig. S5. The photovoltaic parameters including the current density (J_{SC}), voltage (V_{OC}), fill factor (FF) and power conversion efficiency (η) of this study have been summarized in Table S4. To study the charge-transfer process taking place at the interface, EIS spectra of DSSC fabricated using pristine Fe_2O_3 and F-Fe_2O_3 are shown in Fig. 6d. Well-defined semicircles representing the charge transfer resistance occurring between the Pt counter electrode and the redox electrolyte (I^-/I_3^-) system are observed in the high frequency region for pristine and F- Fe_2O_3 photoanodes based DSSCs. The charge transfer resistance is higher in case of F-Fe_2O_3 compared to pristine and thus it can be inferred that the former has a lower recombination rate. Furthermore, the electron lifetime, τ_n was calculated

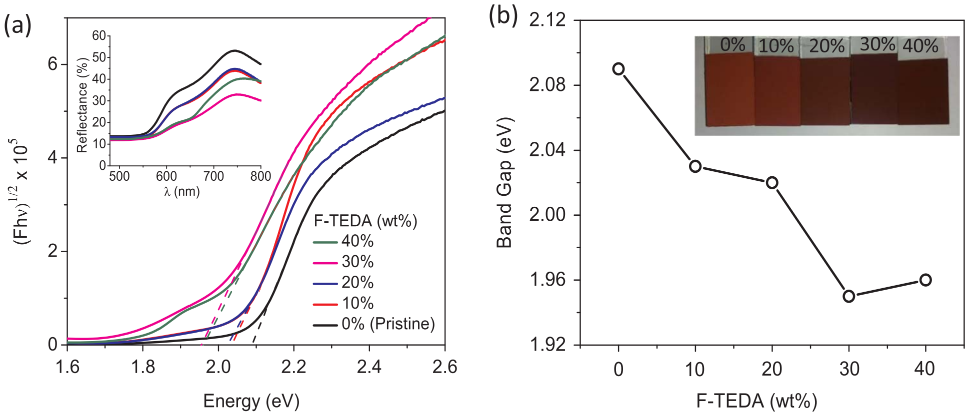

Fig. 5. (a) Tauc plots of pristine and F-$Fe_2O_3$with UV–VisUV-vis diffuse reflectance spectra (inset, a) (b) Variation in bandgap values of α-Fe_2O_3 upon fluorination. The digital photographs of films are shown in inset.

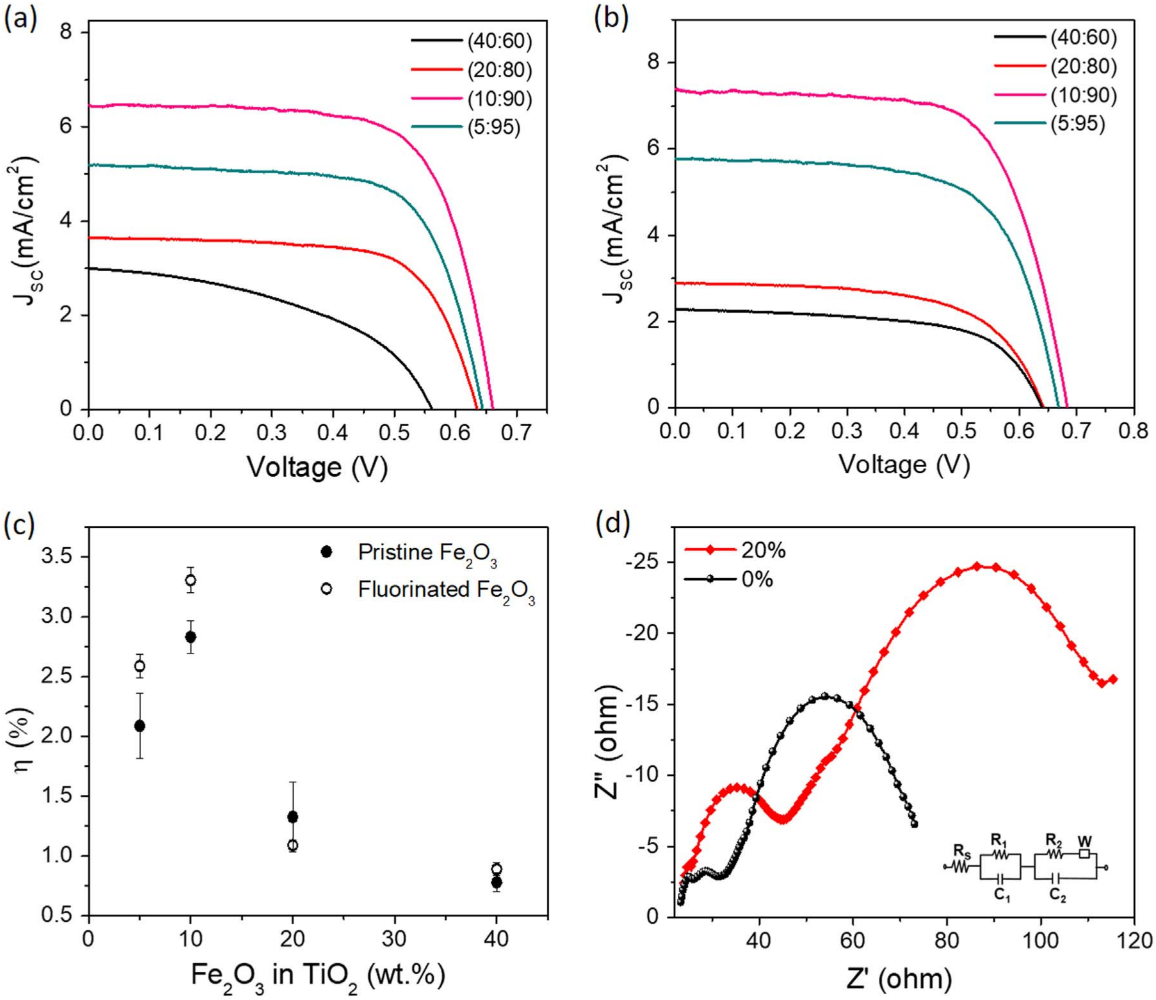

Fig. 6. J-V characteristics of (a) pristine α-Fe_2O_3 and (b) 20% F-Fe_2O_3 photoanode mixed in different weight ratios with TiO_2 (P25) as photoanode. (c) Photo-conversion efficiency (d) Nyquist plot of the optimized composition (10% of Fe_2O_3 in TiO_2) for pristine and F-Fe_2O_3 respectively. Inset shows an equivalent circuit diagram.

to be 0.074 ms and 0.044 ms ($\tau_n = R_1 \times C_1$) for pristine and F-Fe_2O_3 respectively.

The photo-electrochemical measurements of the α-Fe_2O_3 films were performed in 1.0 M aqueous KOH solution (pH = 13.6) under 100 W/m^2 light illumination as shown in Fig. 7a (see Fig. S5 for dark current). α-Fe_2O_3 films were prepared by screen printing a layer of optimized thickness of ~10 µm (Fig. S6) and annealing temperature of ~500 °C for maximum photoresponse (Fig. S7). The pristine α-Fe_2O_3 exhibit a photocurrent density of 0.14 µA cm^{-2} at 1.23 V versus RHE. The current density for pristine α-Fe_2O_3 is very low due to the high bulk resistance as well as interfacial resistance of dendritic α-Fe_2O_3 nanostructures resulting in charge carrier accumulation at the surface leading to re-combination losses (Fig. S8). However, it is interesting to study the relative changes in the current density upon fluorination. The J-V characteristic curves in Fig. 7a shows a systematic increase in photocurrent over the entire voltage range upon fluorination upto 30% of F-TEDA beyond which it decreases. The light on-off current taken at 1.6 V versus Ag/AgCl clearly shows the trend observed for 10%, 20% and 30% of F-TEDA while it is lowered at 40% of F-Fe_2O_3 which is related to the lower at% of F atoms as seen from the XPS analysis (Fig. 7b and c). Otherwise, F-Fe_2O_3 with preferred (110) orientation and lowered bandgap is expected to show a higher photo-electrochemical activity with respect to pristine α-Fe_2O_3. The increase in photocurrent at higher at% of F (Fig. 7d) may be attributed to the fact that F atoms generate charge imbalances at Fe_2O_3 surface resulting in a slower re-combination of the electron-hole pairs [40]. The electron and holes are thus available at surface and have the better opportunity to react with water.

Mott-Schottky measurements were carried out using electrochemical impedance spectroscopy to elucidate the effect of fluorine on the mechanism of the visible light induced photoactivity (Fig. 8a). The Mott–Schottky plots are extrapolated to the *x*-axis to calculate the respective conduction band edge in all cases. Pristine α-Fe_2O_3 yielded a conduction band edge of 0.41 V versus RHE, in agreement with previously reported values [45]. The valence band position is also calculated by adding the value of band gap (obtained from UV-DRS measurements) to conduction band edge. The band structure consisting of the conduction band, the approximate position of the mid-band gap energy level, and the valence band of pristine and F-Fe_2O_3 are shown in Fig. 8b. The effect of surface fluorination is clearly visible from the shift observed in the conduction band edge from 0.41 V (pristine) to 0.52 V versus RHE of F-Fe_2O_3 with higher wt% of F-TEDA. The lowering of conduction band level (positive position) and increase in photocurrent density may be attributed to increase in surface charge density upon fluorination. The carrier densities (N_d) calculated from slopes of Mott–Schottky plots of the doped samples are within the same order of magnitude (~10^{19}) including pristine α-Fe_2O_3 (Table S6). The surface fluorine is not an actual dopant however its surface attachment contributes to lowering of flat-band potential for enhancing the photo-electrochemical process.

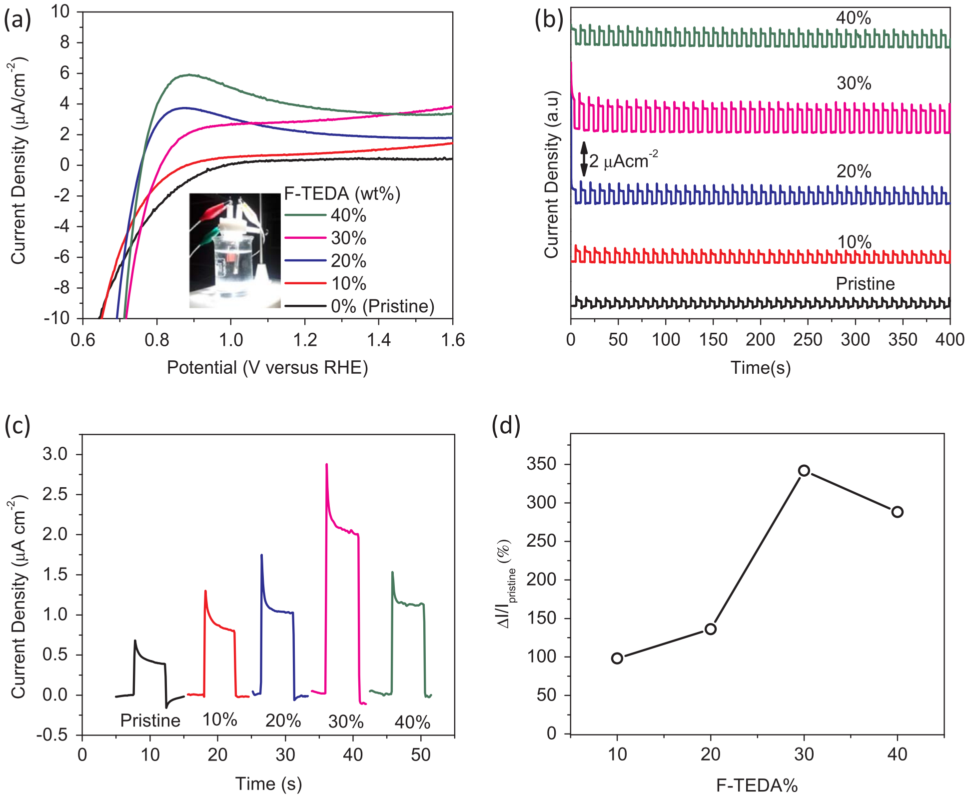

Fig. 7. (a) J-V characteristics of α-Fe_2O_3 films in light (100 W/m^2). Inset shows the set up used for measurements. (b) Chrono-amperometric measurements performed at 1.6 V versus RHE. (c) I-t curve of pristine and fluorinated Fe_2O_3 films on exposure to light for 5 s. (d) The photocurrent response with respect to pristine Fe_2O_3 films.

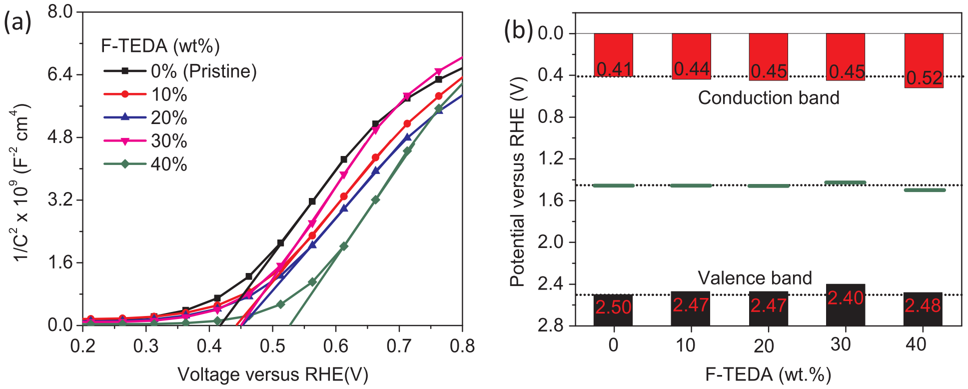

Fig. 8. (a) Mott–Schottky plots of pristine α-Fe_2O_3 and F-Fe_2O_3. The intercept of the linear extrapolation with the *x*-axis (potential) marks the flat-band potential as $(U_{fb} + \frac{K_bT}{e})$. (b) Band structure of the synthesized α-Fe_2O_3 with different quantity of F-TEDA. Conduction band (red bars), the approximate position of the mid-band gap energy level (green line), and the valence band (black bars). (For interpretation of the references to color in this figure legend, the reader is referred to the web version of this article).

4. Conclusions

In summary, we have studied the structural, optical and photoelectrochemical effect of surface fluorination of dendritic α-Fe_2O_3 nanostructures. Selectfluor (F-TEDA) is used as a easy and safe reagent for fluorination of Fe_2O_3. The growth process is accelerated along the preferred [110] direction in presence of F-TEDA as the fluorinating agent. As a result of surface fluorination, there is a significant improvement in the optical properties in terms of lowering of band gap of α-Fe_2O_3. The effect of fluorination is visible in improved performance in dye sensitized solar cells and higher current density in photoelectrochemical cell. The synthesis method developed in this study could be further extended to fluorination of other metal oxides for energy-storage devices and water treatment applications. The morphological tailoring of α-Fe_2O_3 using F-TEDA can also be applied to other metal oxides which will be explored in future studies.

Acknowledgements

Authors acknowledge CeNS, Bangalore for FESEM characterization and the Material Research Centre, MNIT Jaipur, India for TEM and XPS characterization facility. The work was partially supported by Department of Science and Technology (SR/FT/CS-144/2011), Govt. of India, and the Indo-Portuguese Program of Corporation in Science and Technology (INT/Portugal/PO2/2013). RG thanks IIT Jodhpur for Seed Grant (I/SEED/RG/20150033).

Appendix A. Supplementary material

Supplementary data associated with this article can be found in the online version at http://dx.doi.org/10.1016/j.solmat.2017.09.006.

References

[1] J. Chen, L. Xu, W. Li, X. Gou, α-Fe_2O_3 nanotubes in gas sensor and lithium-ion battery applications, Adv. Mater. 17 (2005) 582–586.

[2] Z. Wang, D. Luan, S. Madhavi, C.M. Li, X.W.D. Lou, α-Fe_2O_3 nanotubes with superior lithium storage capability, Chem. Commun. 47 (2011) 8061–8063.

[3] P. Tartaj, M. Del Puerto Morales, S. Veintemillas-Verdaguer, T. González-Carreño, C.J. Serna, The preparation of magnetic nanoparticles for applications in biomedicine, J. Phys. D. Appl. Phys. 36 (2003) R182–R197.

[4] T.W. Hamann, Splitting water with rust: hematite photoelectrochemistry, Tetrahedron 67 (2011) 8639–8647.

[5] K. Sivula, F. Le Formal, M. Grätzel, Solar water splitting: progress using hematite (α-Fe_2O_3) photoelectrodes, ChemSusChem 4 (2011) 432–449.

[6] Y. Jiao, Y. Liu, F. Qu, X. Wu, Dendritic α-Fe_2O_3 hierarchical architectures for visible light driven photocatalysts, CrystEngComm 16 (2014) 575–580.

[7] S. Zeng, K. Tang, T. Li, Z. Liang, D. Wang, Y. Wang, W. Zhou, Hematite hollow spindles and microspheres: selective synthesis, growth mechanisms, and application in lithium ion battery and water treatment, J. Phys. Chem. C 111 (2007) 10217–10225.

[8] J. Peng, C.C. Chai, A study of the sensing characteristics of Fe_2O_3 gas-sensing thin film, Sens. Actuators B 13–14 (1993) 591–593.

[9] Y. Kim, J.-H. Pee, J.H. Chang, K. Choi, K.J. Kim, D.Y. Jung, Silica effect on coloration of hematite nanoparticles for red pigments, Chem. Lett. 38 (2009) 842–843.

[10] M.H. Lee, J.H. Park, H.S. Han, H.J. Song, I.S. Cho, J.H. Noh, K.S. Hong, Nanostructured Ti-doped hematite (α-Fe_2O_3) photoanodes for efficient photoelectrochemical water oxidation, Int. J. Hydrog. Energy 39 (2014) 17501–17507.

[11] M. Shimojo, M. Takeguchi, K. Furuya, Formation of crystalline iron oxide nanostructures by electron beam-induced deposition at room temperature, Nanotechnology 17 (2006) 3637–3640.

[12] T. Tepper, C.A. Ross, Pulsed laser deposition of iron oxide films, J. Appl. Phys. 91 (2002) 4453–4456.

[13] P.A.K. Elttayef, A. Prof, M.H. Jaduaa, M.A. Muhammed, Study the structural and optical properties of Fe_2O_3 thin films prepared by RF magnetron, Int. J. Appl. Innov. Eng. Manag. 4 (2015) 99–105.

[14] F.J. Morin, Electrical properties of alpha Fe_2O_3, Phys. Rev. 93 (1954) 1195–1199.

[15] J.H. Kennedy, K.W. Frese, Photooxidation of water at α-Fe_2O_3 electrodes, J. Electrochem. Soc. 125 (1978) 709–714.

[16] N.J. Cherepy, D.B. Liston, J.A. Lovejoy, H. Deng, J.Z. Zhang, Ultrafast studies of photoexcited electron dynamics in γ- and α-Fe_2O_3 semiconductor nanoparticles, J. Phys. Chem. B 102 (1998) 770–776.

[17] I. Cesar, K. Sivula, A. Kay, R. Zboril, M. Grätzel, Influence of feature size, film thickness, and silicon doping on the performance of nanostructured hematite photoanodes for solar water splitting, J. Phys. Chem. C 113 (2009) 772–782.

[18] J.B. Goodenough, Metallic oxides, Prog. Solid State Chem. 5 (1971) 145–399.

[19] J. Lian, X. Duan, J. Ma, P. Peng, T. Kim, W. Zheng, Hematite (α-Fe_2O_3) with various morphologies: ionic liquid-assisted synthesis, formation mechanism, and properties, ACS Nano 3 (2009) 3749–3761.

[20] C. Yilmaz, U. Unal, Morphology and crystal structure control of α-Fe_2O_3 films by hydrothermal-electrochemical deposition in the presence of Ce^{3+} and/or acetate, F^- ions, RSC Adv. 6 (2016) 8517–8527.

[21] G.G. Amatucci, N. Pereira, Fluoride based electrode materials for advanced energy storage devices, J. Fluor. Chem. 128 (2007) 243–262.

[22] H. Kim, W. Choi, Effects of surface fluorination of TiO_2 on photocatalytic oxidation of gaseous acetaldehyde, Appl. Catal. B Environ. 69 (2007) 127–132.

[23] H. Park, W. Choi, Effects of TiO_2 Surface fluorination on photocatalytic reactions and photoelectrochemical behaviors, J. Phys. Chem. B 108 (2004) 4086–4093.

[24] Y. Wang, G. Cheng, Y. Zhang, H. Ke, C. Zhu, Synthesis of fluorinated SnO_2 3D hierarchical structures assembled from nanosheets and their enhanced photocatalytic activity, RSC Adv. 5 (2015) 88079–88086.

[25] A. Gasparotto, D. Barreca, D. Bekermann, A. Devi, R.A. Fischer, P. Fornasiero, V. Gombac, O.I. Lebedev, C. Maccato, T. Montini, G. Van Tendeloo, E. Tondello, F-doped Co_3O_4 photocatalysts for sustainable H_2 generation from water/ethanol, J. Am. Chem. Soc. 133 (2011) 19362–19365.

[26] K. Karthikeyan, S. Amaresh, S.N. Lee, V. Aravindan, Y.S. Lee, Fluorine-doped Fe_2O_3 as high energy density electroactive material for hybrid supercapacitor applications, Chem. Asian J. 9 (2014) 852–857.

[27] V.L. Sophronov, M.E. Kalaev, Y.N. Makaseev, V.I. Sachkov, V.V. Verkhoturova, Study on the process of Fe (III) oxide fluorination, IOP Conf. Ser. Mater. Sci. Eng. 110 (2016) 12069.

[28] M. Cao, T. Liu, S. Gao, G. Sun, X. Wu, C. Hu, L.W. Zhong, Single-crystal dendritic micro-pines of magnetic α-Fe_2O_3: large-scale, Synth. Form. Mech. Prop. Angew. Chem. Int. Ed. 44 (2005) 2–6.

[29] K.P. Shejale, D. Laishram, R.K. Sharma, High-performance dye-sensitized solar cell using dimensionally controlled titania synthesized at sub-zero temperatures, RSC Adv. 6 (2016) 23459–23466.

[30] R.E. Banks, R.G. Syvretb, l-Alkyl-4-fluoro-l,4-diazoniabicyclo[2.2.2]octane Salts: a novel family of electrophilic fluorinating agents, J. Chem. Soc., Chem. Commun. (1992) 595–596.

[31] G.S. Lal, G.P. Pez, R.G. Syvret, Electrophilic NF fluorinating agents, Chem. Rev. 96 (1996) 1737–1756.

[32] R.E. Banks, M.K. Besheesh, S.N. Mohialdin-khaffaf, I. Sharif, N-Halogeno compounds. Partl8. l-Alky1-4-fluoro-l,4 diazoniabic yclo [2.2.2] octane salts: user-friend1y site-selective electrophilic fluorinating agents of the N-fluoroammonium class, J. Chem. Soc., Perkin Trans. 1 (1996) 2069–2076.

[33] J.J. Hart, R.G. Syvret, Industrial scale production of Selectfluor™ fluorination agent: from initial concept to full scale commercial production in a 5 year period, J. Fluor. Chem. 100 (1999) 157–161.

[34] P.T. Nyffeler, S.G. Duron, M.D. Burkart, S.P. Vincent, C.H. Wong, Selectfluor: mechanistic insight and applications, Angew. Chem. Int. Ed. 44 (2004) 192–212.

[35] A.E. Green, C.-Y. Chiang, H.F. Greer, A. Waller, A. Ruszin, J. Webster, Z. Niu, K. Self, W. Zhou, Growth mechanism of dendritic hematite via hydrolysis of ferricyanide, Cryst. Growth Des. 17 (2017) 800–808.

[36] C. Wang, Y. Zhang, Y. Li, J. Liu, Q. Wu, Synthesis of fluorine-doped α-Fe_2O_3 nanorods toward enhanced lithium storage capability, Nanotechnology 28 (2017) 65401.

[37] T. Nakau, Electrocal conductivity of Fe_2O_3, J. Phys. Soc. Jpn. 15 (1960) 727.

[38] N. Iordanova, M. Dupuis, K.M. Rosso, Charge transport in metal oxides: a theoretical study of hematite α-Fe_2O_3, J. Chem. Phys. 122 (2005) 144305.

[39] J. Cai, S. Li, Y. Liu, M. Gao, D. Wang, G. Qin, Orientation modulated charge transport in hematite for photoelectrochemical water splitting, Funct. Mater. Lett. 9 (2016) 1650047.

[40] L.P. Zhu, L.L. Wang, N.C. Bing, C. Huang, L.J. Wang, G.H. Liao, Porous fluorine-doped α-Fe_2O_3 hollow spheres: synthesis, growth mechanism, and their application in photocatalysis, ACS Appl. Mater. Interfaces 5 (2013) 12478–12487.

[41] A. Annamalai, P.S. Shinde, T.H. Jeon, H.H. Lee, H.G. Kim, W. Choi, J.S. Jang, Fabrication of superior α-Fe_2O_3 nanorod photoanodes through ex-situ Sn-doping for solar water splitting, Sol. Energy Mater. Sol. Cells 144 (2016) 247–255.

[42] J.C. Yu, J. Yu, W. Ho, Z. Jiang, L. Zhang, Effects of F-doping on the photocatalytic activity and microstructures of nanocrystalline TiO_2 powders, Chem. Mater. 14 (2002) 3808–3816.

[43] M. Shahpari, A. Behjat, M. Khajaminian, N. Torabi, The influence of morphology of hematite (α-Fe_2O_3) counter electrodes on the efficiency of dye-sensitized solar cells, Sol. Energy 119 (2015) 45–53.

[44] W. Yang, X. Xu, Z. Li, F. Yang, L. Zhang, Y. Li, A. Wang, S. Chen, Construction of efficient counter electrodes for dye-sensitized solar cells: Fe_2O_3 nanoparticles anchored onto graphene frameworks, Carbon 96 (2016) 947–954.

[45] P. Saurabh Bassi, L. Helena Wong, J. Barber, Iron based photoanodes for solar fuel production, Phys. Chem. Chem. Phys. 16 (2014) 11834–11842.